Epitaxial $Fe_{3-x}Ti_xO_4$ films from magnetite to ulvöspinel by pulsed laser deposition

T.C. Droubay[1*], C.I. Pearce[1], E.S. Ilton[1], M.H. Engelhard[1], W.Jiang[1], S.M. Heald[2], E. Arenholz[3], and K.M. Rosso[1]

[1] *Fundamental and Computational Sciences Directorate, Pacific Northwest National Laboratory, Richland, WA 99352 USA*

[2] *Advanced Photon Source, Argonne National Laboratory, Argonne, IL 60439 USA*

[3] *Advanced Light Source, Lawrence Berkeley National Laboratory, Berkeley, CA 94720 USA*

Epitaxial films along the $Fe_{3-x}Ti_xO_4$ (titanomagnetite) compositional series from pure end-members magnetite (Fe_3O_4) to ulvöspinel (Fe_2TiO_4) were successfully grown by pulsed laser deposition on MgO(100) substrates. Spectroscopic characterization including high resolution x-ray diffraction, x-ray photoelectron spectroscopy, and synchrotron-based x-ray absorption and magnetic circular dichroism consistently shows that Ti(IV) substitutes for Fe(III) in the inverse spinel lattice with a proportional increase in lattice Fe(II) concentration. No evidence of Ti interstitials, spinodal decomposition, or secondary phases was found in the bulk of the grown films. At the uppermost few nanometers of the Ti-bearing film surfaces, evidence suggests that Fe(II) is susceptible to facile oxidation, and that an associated lower Fe/Ti ratio in this region is consistent with surface compositional incompleteness or alteration to a titanomaghemite-like composition and structure. The surface of these films nonetheless appear to remain highly ordered and commensurate with the underlying structure despite facile oxidation, a surface condition that is found to be reversible to some extent by heating in low oxygen environments.

I. INTRODUCTION

Iron oxides as a general class of materials have been studied extensively due to their potential technological use as well as their ubiquitous presence in soils. Among the iron oxides, ferrimagnetic spinel thin films have received considerable attention for prospective applications in microwave, magnetic storage, and spintronic devices.[1-3] Oxide spinel structure materials have the formula AB_2O_4, in which tetrahedral (A) and octahedral (B) cations occupy some or all of the sites within a face-centered cubic close-packed lattice of oxygen anions. In the case of iron oxide inverse spinels (Fe_2MO_4, M=Fe, Co, Ni, Mn, Zn, etc.), trivalent cations are split between the A and B sites and divalent cations occupy only the B sites. The A- and B-site cation composition and distribution is critically important for the resulting electrical, magnetic, and redox properties of the material.

The present study deals with epitaxial growth of $Fe_{3-x}Ti_xO_4$ thin films, compositionally controlled along the binary solid-solution series from pure Fe_3O_4 magnetite (x=0.0) to Fe_2TiO_4 ulvöspinel (x=1.0). Intermediate compositions ($0.0<x<1.0$) are referred to as titanomagnetites. End-member magnetite is the archetypal ferrimagnet, in which high-spin iron cations are distributed ($Fe^{3+}{}_A(Fe^{2+},Fe^{3+})_BO_4$) with opposing A- and B-site spin sublattices, imparting a net 4 μ_B magnetization per formula unit. Systematic Ti substitution for Fe, nominally Ti(IV) for Fe(III), is attractive from the standpoint that it also proportionally increases lattice Fe(II) concentration for charge balance and reduces the net ferrimagnetic moment. However, the Ti/Fe cation site distribution and formal oxidation states remain somewhat controversial in practice. Based on magnetization measurements, electrical transport, and thermoelectric data obtained from bulk solid solutions or bulk single crystals[4-5] several conflicting x-dependent cation distribution models have been presented.[4,6-11] While these models are certainly relevant to the

present study, inferences made from bulk materials are not always applicable to systems with nanoscale dimensionality such as thin films.[12-13] It is thus of general scientific interest and potential technological value to examine and attain controlled thin film synthesis of this binary series.

There have been very few reported studies of epitaxial thin film growth along the magnetite-ulvöspinel series. Possible reasons include lack of readily available pure bulk end members for deposition precursor materials, and challenges with spinodal decomposition at synthesis temperatures below the bulk consolute temperature (~ 490°C for bulk phases)[14]. However, epitaxial Fe_3O_4 films have been successfully made for many years by a variety of deposition techniques, as reviewed by Chambers,[15] including by pulsed laser deposition (PLD).[13,16-19] But in contrast to the substantial work on magnetite, to the best of our knowledge only one group has reported titanomagnetite thin film synthesis. Murase *et al.* prepared and investigated solid-solution $0.4Fe_3O_4{\cdot}0.6Fe_2TiO_4$ films using either MgO(100) or α-Al_2O_3(0100) substrates.[20-21]

In the present paper, we report successful growth of epitaxial $Fe_{3-x}Ti_xO_4$ thin films from pure magnetite to ulvöspinel by PLD. MgO(100) substrates were chosen because of prior success with magnetite and the relatively small lattice mismatch. The unit cell dimensions of Fe_3O_4 (8.396 Å) and Fe_2TiO_4 (8.544 Å) are nominally twice that of MgO (4.212 Å), resulting in lattice mismatches of only –0.33% and 1.4% respectively. We present PLD synthesis growth conditions as well as detailed bulk and surface characterization of the thin films by reflection high energy electron diffraction (RHEED), x-ray photoelectron spectroscopy (XPS), K- and L-edge x-ray absorption near-edge spectroscopy (XANES), high resolution x-ray diffraction (HRXRD), and x-ray magnetic circular dichroism (XMCD).

II. EXPERIMENT

We developed PLD protocols for thin film growth targeted to the following five compositions, x=0.00, 0.25, 0.50, 0.75, and 1.00. Two main targets were used, depending upon the desired Ti concentration, an α-Fe_2O_3 target and an Fe_2TiO_4 target. The latter was a pressed and sintered ceramic PLD target. An additional pure TiO_2 target was also used for a few growths to confirm the solid solubility and homogeneity of Ti in the magnetite lattice. All targets were 2" diameter, and commercially purchased from the Kurt J. Lesker Company. The laser spot (~1×10 mm^2) from a KrF laser (248 nm) was rastered across a rotating target while the substrate was also rotating, allowing for uniform thickness across the substrate. Prior to growth, all targets were ablated for 15 minutes at a laser repetition rate of 10 Hz in 10 mTorr O_2 to eliminate carbonaceous surface contamination. Further laser-induced reduction of the Fe_2O_3 target was performed by ablating it at < 1×10^{-8} Torr O_2 for an additional 30 minutes prior to growth. A computer-controlled combination of laser pulses at the two different targets was calibrated and used when a stoichiometry other than the endmembers was desired. In a typical two-target growth procedure, a few laser pulses would ablate one target and then do same on the other, separated by closing the laser shutter in-between while the second target was moved into position. The sequence would be repeated as many times as necessary to achieve the film thickness sought, in this case nominally ~50-100 nm. Intermediate composition $Fe_{3-x}Ti_xO_4$ films with Ti concentrations of x=0.25, 0.50, and 0.75 were routinely grown in this way.

Single-side epi-polished 10×10×1 mm^3 or 10×10×0.5 mm^3 MgO(100) substrates were used for all growths. As-received MgO substrates were initially etched in H_3PO_4, rinsed in de-ionized water, and annealed under O_2 according to the procedure shown by Perry *et al*. to result in atomically flat, well-ordered, crystalline surfaces.[22-23] Substrates were ultrasonically washed in

isopropanol and methanol before introduction into the vacuum chamber. After sample introduction and prior to growth, the substrates were heated up to 500°C in 10 mTorr O_2 to eliminate adventitious carbon from the growth surface. Oxygen flow into the chamber was stopped and the chamber pumped down prior to commencing PLD.

The oxygen partial pressure in the deposition chamber during film growth was < 3×10^{-9} Torr. The substrate temperature for all growths was ~350°C, using a laser repetition rate of 2 Hz. Temperature, laser repetition rate, and oxygen partial pressure were chosen based on previous studies to eliminate Mg out-diffusion into the film during deposition from the underlying MgO substrate. For example, previous Fe_3O_4/MgO(100) deposition studies report significant film-substrate reaction and Mg out-diffusion at temperatures in excess of ~350°C.[24-25] Also, reports on the growth of Fe_3O_4 by PLD addressed the dependence of surface morphology and magnetic properties on pressure.[18] Molten droplets and large particles ejected from the target during the laser ablation process are strongly forward directed along the on-axis position. Elimination of the large particles is accomplished through growing in a background gas N_2 and by using an off-axis configuration, as was adopted here. No significant differences in structural quality or Ti incorporation were observed in films deposited in either pressures of 1×10^{-7} Torr or 10 mTorr of N_2.

Several characterization methods required exposure to ambient atmosphere, but were presumed insensitive to surface oxidation. Air exposure was always minimized to just that involving sample transport or shipping. HRXRD was used to investigate the crystallinity, cell parameter, and detailed microstructure of the films and was performed in air. XANES was performed in air on the PNC-CAT insertion device (20-ID) beamline at the Advanced Photon Source located at Argonne National Laboratory. *K*-edge XANES is a sensitive probe of both the

Fe and Ti oxidation states in the film bulk, and provides qualitative information on their lattice location. Sample rotation about the surface normal was used to minimize Bragg diffraction effects and spectra collected with crossed (perpendicular and parallel) polarizations, relative to the sample surface, were appropriately averaged such that the XANES of the epitaxial films could be directly compared with those measured for metal foil(s) and oxide powder standards.

XPS of plasma-cleaned films that had been stored in an N_2 glove-box atmosphere was performed in a Gammadata/Scienta SES 200 photoelectron spectrometer with a monochromatic Al-Kα (1486.7 eV) x-ray source. The angle between the x-ray beam and the axis of the analyzer is fixed at the "magic angle" of ~54°, while the photoelectron emission angle can be varied between normal emission (bulk sensitive) and grazing emission (surface sensitive). RHEED was performed in a sample preparation chamber appended to the Scienta XPS system. Prior to RHEED analysis, adventitious carbon was cleaned from the sample surface using an electron cyclotron resonance oxygen plasma unit. The films were then reduced in vacuum by annealing to ~350 °C. *In-situ* heating experiments, under vacuum (~5×10^{-9} Torr), with a hydrogen partial pressure at $4.6\text{x}10^{-9}$ Torr in the XPS chamber were also performed on the as-synthesized films at 100˚C and 350˚C, in order to restore surface stoichiometry, using a Physical Electronics Quantum 2000 Scanning ESCA Microprobe. This Physical Electronics system uses a focused monochromatic Al-Kα x-ray source and a spherical section electron energy analyzer. The instrument has a 16-element multichannel detection system. A 105 W x-ray beam focused to 100 μm diameter was rastered over a 1.4 mm × 0.3 mm rectangle on the sample. The x-ray beam is incident normal to the sample and the photoelectron detector is at 45° off-normal, restricting the probing depth to the near surface (~$3\lambda\cos\theta$), where λ is the inelastic mean free path of the electrons and θ is the emission angle measured from the surface normal. The high energy

resolution data was collected using a pass-energy of 46.95 eV with a step size of 0.125 eV. For the Ag $3d_{5/2}$ line, these conditions produced a FWHM of 0.98 eV. Regional scans of the Fe 2*p*, O 1*s*, Ti 2*p*, and C 1*s* region were recorded, and the energy scale was referenced to adventitious C 1*s* at 285.0 eV. The Fe 2*p* were best fit by nonlinear least-squares using the CasaXPS curve resolution software, as described in the Supplemental Information section of Ilton *et al*.[26].

Films were also heated at 300˚C on a hot plate for 10 minutes in an N_2 glove-box atmosphere, to restore surface stoichiometry and $L_{2,3}$-edge x-ray absorption and XMCD spectra were collected with circularly polarized light on beamline 4.0.2 at the Advanced Light Source (ALS) located at Lawrence Berkeley National Laboratory, using the eight-pole magnet end station[27]. The films were mounted on the copper sample manipulator with carbon tape and silver paint and loaded into the end station under anoxic conditions. Spectra were collected at 140 K. The XAS signal was monitored in total electron yield (TEY) mode, giving an effective probing depth of ~40-50 Å, poorly quantifiable due to the uncertainty in the specific processes in the source of the signal.[28] At each energy point, the XAS was measured for the two opposite magnetization directions by reversing the applied field of 0.6 T. The XAS spectra of the two magnetization directions were normalized to the incident beam intensity and subtracted from each other to obtain the XMCD spectrum.[29] For intermediate (titanomagnetite) compositions, XMCD spectra have four main peaks in the Fe L_3 edge with positive, negative, positive, and negative signals, which are related to the amounts of Fe d^6 *Td* (~707 eV), d^6 *Oh* (708 eV), d^5 *Td* (~709 eV), and d^5 *Oh* (~710 eV), respectively.[30] End-member magnetite does not contain an Fe d^6 *Td* component. To obtain the cation distribution over the three (magnetite) or four (titanomagnetite) Fe sites, measured XMCD spectra were fitted by means of a nonlinear least-squares analysis, using theoretical spectra previously calculated at the quantum mechanical level

for each site. In these calculations, described in van der Laan and Kirkman[31] and van der Laan and Thole[32], 10Dq crystal field parameters were taken as 1.2 and 0.6 eV for Fe *Oh* and *Td* sites. The results were convoluted by a Lorentzian of 0.3 (0.5) eV for the L_3 (L_2) edge to account for intrinsic core-hole lifetime broadening and by a Gaussian of 0.2 eV to account for instrumental broadening.

III. RESULTS & DISCUSSION

A. Film crystallinity and microstructure

Successful synthesis of phase-pure epitaxial $Fe_{3-x}Ti_xO_4$ films with high crystallinity and minimal microstructure depends on choice of substrate, laser repetition rate, temperature, and partial pressure of oxygen during deposition. The three most common substrates for the deposition of epitaxial Fe_3O_4 historically have been MgO, $MgAl_2O_4$, and α-Al_2O_3. Sapphire, α-Al_2O_3(001), substrates were avoided because they tend to yield nanoscale phase separation at the interface.[33] MgO(100) was deemed the most suitable substrate to minimize any interfacial strain-induced effects because of its small lattice mismatch with Fe_3O_4(100), as documented by Parames *et al*.[34] With respect to oxygen partial pressure, it was found that $Fe_{3-x}Ti_xO_4$ grew best at $< 3\times10^{-9}$ Torr. Film thicknesses ranged from 10 nm to ~100 nm. Shown in Fig. 1(a) are the typical RHEED patterns obtained for the initial MgO(100) substrate, following growth of a ~10 nm Fe_2TiO_4/MgO(100) film, and the film after annealing to ~300°C following 30 minutes in an electron cyclotron resonance oxygen plasma to clean off adventitious carbon. As seen in the streaky RHEED pattern from the annealed film following plasma-cleaning, the surface is exceptionally flat and well-ordered. Only pure Fe_3O_4 exhibits quarter-order streaks (not shown) along [100] relative to MgO, consistent with the reported $\bar{}$ $\bar{}$ R45° magnetite (100)

surface reconstruction (Fig. 1b).[35-36] With the addition of Ti, none of the grown films $Fe_{2.75}Ti_{0.25}O_4$, $Fe_{2.5}Ti_{0.5}O_4$, $Fe_{2.25}Ti_{0.75}O_4$, nor Fe_2TiO_4 (100) are found to exhibit this reconstruction, suggesting perhaps a bulk (polar) termination (e.g., Pentcheva *et al.*[37]). Curiously, upon exposure to significant oxygen or ambient atmosphere, the surface appears to roughen, as seen in the modulation along the RHEED streaks but does not appear to convert phase as seen for pure Fe_3O_4 upon exposure to water vapor.[38]

The structural quality of the films is confirmed with HRXRD, as illustrated for $Fe_{2.75}Ti_{0.25}O_4$ (Fig. 2a) and $Fe_{2.25}Ti_{0.75}O_4$ (Fig. 2b), which reveal (100) oriented films with high crystallinity and minimal mosaic spread. Two distinct Bragg peaks are visible at Ω = ~42.5° and 42.8° in Fig. 2a corresponding to the titanomagnetite film and MgO, respectively. And as can be seen by comparison of HRXRD spectra for the two stated $Fe_{3-x}Ti_xO_4$ films, the Bragg peak associated with the film shifts to lower angle as the Ti concentration increases. This decrease in the Bragg angle corresponds to an increasing unit cell dimension with increasing Ti content, consistent with expectations from related studies of the bulk phases.[30] An epitaxially-induced tetragonal distortion is expected on use of MgO(100) substrates because of the small but finite lattice mismatch.[15] The out-of-plane lattice parameters measured by HRXRD increase from 8.434 Å to 8.492 Å as x increases from x = 0.25 to x = 0.75, which is a very similar increase to that seen in the corresponding bulk phases.[30] From the combined RHEED and HRXRD data, it can be concluded that the $Fe_{3-x}Ti_xO_4$ films grow epitaxially on the MgO substrate with the desired inverse spinel crystal structure and (100) surface orientation. In addition, we can infer from the monotonic change in lattice constant with titanium concentration that the majority of Ti atoms are substituting for Fe in the cationic sublattice. Within the sensitivity of HRXRD, there is no

indication of either secondary phases or spinodal decomposition to distinct Fe_3O_4 and Fe_2TiO_4 phases within any of the $Fe_{3-x}Ti_xO_4$ films.

B. Bulk film cation charge state and local structure

While phase separation to domains larger than ~5-10 nm would have been detected by HRXRD, finer-scale separation could have been overlooked. Fe and Ti *K*-edge XANES with fluorescence detection was therefore used as a more effective probe of the atomic structure. Because this technique is able to probe the entire film in addition to being element-specific, it provides information on Ti and Fe oxidation states as well as the local structure around these cations in the bulk of the film.

Figure 3a shows Ti *K*-edge XANES for three different $Fe_{3-x}Ti_xO_4$/MgO(100) films. By comparing the inflection point of the Ti absorption spectra with those from Ti standards, it is clear that Ti is in the +4 formal charge state in all of the titanomagnetite films, regardless of Ti concentration up to and including Fe_2TiO_4. For example, shown in the inset to Figure 3a is an absorption edge and overall lineshape comparison of Fe_2TiO_4 with that from TiO_2 powder. Edge position comparisons for all grown Ti-bearing film compositions confirm the designation of Ti(IV) throughout the films. Furthermore, because of apparent differences in the overall lineshape, the majority of Ti in the films is not from a secondary phase such as TiO_2, although the presence of small amounts of this phase at the surface cannot be ruled out. This is also true of a separate Fe_2TiO_4/MgO(100) film grown by PLD using Fe_2O_3 and TiO_2 targets, establishing that small amounts of phase separation nominally expected in a typical pressed and sintered ceramic target (e.g., the commercial Fe_2TiO_4 PLD target) does not lead to phase separation in the resulting film.

Figure 3b shows Fe *K*-edge XANES from the same three epitaxial titanomagnetite thin films as in Figure 3a, with the inset showing the powder XANES spectra from multiple standard iron oxide/oxy(hydr)oxide targets in addition to a Fe metal standard. Comparison of the inflection point in the Fe absorption edges recorded for the titanomagnetite films with those from the standards provides a basis to determine an average formal oxidation state for the iron component using FeO for the Fe(II) standard and α-Fe_2O_3 as the Fe(III) standard. In addition, although the Fe XANES spectra from the Fe_2TiO_4 films are offset for clarity, the curves are displaced slightly in energy from each other, indicating that the Fe(II)/Fe(III) ratio systematically increases with increasing Ti concentration as expected.

By comparison of the Ti and Fe x-ray absorption lineshapes from the same films as above, it can be observed that the relatively small pre-edge feature is stronger for the Ti *K*-edge than for the Fe. The pre-edge feature is due to a 1*s* to 3*d* transition which is formally dipole forbidden but increases in intensity through local mixing between the 3*d* and 4*p* states in tetrahedral symmetry.[39-40] In a study of Ti-based catalysts, Thomas and Sankar[41] showed the dependence of the Ti *K*-pre-edge peak intensity on the coordination of the oxygen atoms around the central Ti(IV). However, since the intensity of the pre-edge peak does not increase with Ti concentration, it seems unlikely that this is a result of Ti cations substituting into A sites in the $Fe_{3-x}Ti_xO_4$ film. It is possible that, although Ti(IV) has substituted into the B-site there may be a next-nearest neighboring cation vacancy that promotes tetragonal strain and thus increases the pre-edge peak intensity. Cationic vacancy or interstitial concentrations dependent upon oxygen fugacity have been suggested by Morris *et al.*[42] as a means to reconcile data on the electronic structure of Nb-doped TiO_2. Furthermore, cation vacancies were concluded to be the predominant defects at high oxygen activities by Aggarwal and Dieckmann in titanomagnetites.[43]

It thus appears plausible that a small population of Ti-associated B-site Fe vacancies may explain the presence of the Ti *K*-pre-edge feature. Such a vacancy would break the requirement that the Fe(II) concentration increase concomitantly with Ti(IV) substitution to preserve charge neutrality for that population of sites.

A qualitative measure to further corroborate the XANES and HRXRD evidence that Ti(IV) is predominantly substituting in the cationic sublattice is a comparison of the XANES lineshapes of Fe in pure bulk standard Fe_3O_4, Fe in the Fe_2TiO_4 thin film, and Ti in the Fe_2TiO_4 thin film (Fig. 4a). The absorption edges have been shifted on the energy scale to align their inflection points to facilitate this comparison. Here the Fe_3O_4 lineshape can be seen to be very nearly approximated by a linear combination of that for Ti and Fe from the thin film, consistent with Ti replacement of the Fe(III) component of Fe_3O_4. This provides further confirmation that the films are nearly free from secondary phases and spinodal decomposition within detection limits of the applied techniques.

To quantitatively determine the average Fe oxidation state within the films, a plot of the measured inflection point as a function of x is shown in Figure 4b. The average Fe oxidation state for all of the films can be seen to lie directly along the line determined by FeO and α-Fe_2O_3. However, this analysis also suggests that the average Fe oxidation state is slightly more oxidized than expected from the stoichiometry. For example, the average Fe oxidation state in the Fe_2TiO_4 thin film is estimated to be ~2.2. Although predominantly reduced as expected, when this observation of slight Fe oxidation is combined with the possible presence of a small population of Ti-associated oxygen vacancies, we must consider the possibility that the near-surface of the films are somewhat non-stoichiometric. We therefore performed a range of surface-sensitive spectroscopic analyses as described below.

C. Film surface properties

A possible near-surface composition and structure consistent with the bulk-signal-dominated film measurements is one in which the upper few nanometers are oxidized to Ti(IV)-doped γ-Fe_2O_3 maghemite. Maghemite is the inverse spinel solid-solution end-member of Fe_3O_4 oxidation, and an analogous topotactic binary exists between titanomagnetite-titanomaghemite. Such a surface layer would provide for a higher than expected Fe(III) concentration in the films, a surface unit cell of identical symmetry and approximately equivalent dimensions to the underlying film bulk, and an intrinsic B-site vacancy component consistent with interpretation of the Ti *K*-pre-edge peak intensity. This altered surface layer may act to either passivate the surface or at least slow the oxidation of more reduced films such as Fe_2TiO_4 as seen by some researchers.[44] To investigate the surface layer in more detail, and the potential for surface re-equilibration, the Fe_3O_4 and Fe_2TiO_4 end-member films were examined with XPS and Fe $L_{2,3}$-edge XAS/XMCD before and after heating, either under high-vacuum in an XPS chamber or in an anoxic N_2 atmosphere glove-box (<1 ppm O_2).

For initial XPS analysis, the films were plasma cleaned prior to analysis to remove adventitious carbon. The photoelectron detector was positioned incident normal to the sample to ensure a sampling depth that would include a contribution from the bulk, as well as the oxidized surface. Figure 5 shows XPS regional scan spectra obtained on the Fe_2TiO_4 film for the Fe 2*p* (Fig. 5a), Ti 2*p* (Fig. 5b), and O 1*s* (Fig. 5c) core-levels. The Fe 2*p* lineshape is complex and inherently broad, but can be used to estimate Fe oxidation states by examination of the satellite structure between the Fe $2p^{3/2}$ and the Fe $2p^{1/2}$ peaks.[45] The valley between the $2p^{3/2}$ and the $2p^{1/2}$ peaks is "filled-in" or lacking an easily identifiable peak. In addition, there is a slight

shoulder on the lower binding energy side of the Fe 2$p^{3/2}$ core-level. With these two observations the oxidation state of the Fe near the surface is clearly a mixture of Fe(II) and Fe(III)[24] consistent with partial surface oxidation of the Fe_2TiO_4 film. This is not surprising considering the sample was briefly exposed to air during transfer into the XPS analysis chamber, allowing for surface oxidation and hydroxylation.[38,46] The O 1*s* core-level is likewise consistent with exposure to water vapor due to the presence of a shoulder roughly 1.5 eV to higher binding energy. Unlike Fe 2*p*, the Ti 2*p* core-level lineshape shown in Fig. 5b indicates that the Ti oxidation state is exclusively Ti(IV). Assuming that the inelastic mean free path of electrons photo-ejected from Fe_2TiO_4 by Al-Kα x-rays is essentially identical to that for Fe_3O_4, we expect from prior precedent on XPS of magnetite surface oxidation that the XPS sampling depth using is deeper than the surface oxidation/passivation layer[38]. Therefore, we can conclude that the entirety of the Ti was in the 4+ oxidation state prior to exposure of the film to air.

Figure 6 shows XPS of as-synthesized Fe_3O_4 (Fig. 6a) and Fe_2TiO_4 (Fig. 6b) films before and after heating for 10 minutes under high vacuum (~5×10^{-9} Torr), with an H_2 background gas ($4.6\text{x}10^{-9}$Torr). Here, XPS was performed without plasma cleaning to eliminate any oxidizing effects that could be caused by the oxygen plasma. Also, to enhance surface sensitivity, the photoelectron detector was positioned at 45° off-normal. Heating the Fe_3O_4 film to 100°C results in a subtle but detectable increase in the Fe(II) shoulder intensity, indicating reduction of the initial, slightly oxidized, surface (Fig. 6a). Estimates of the surface Fe(II) concentration before and after heating are 30% Fe(II) before, and 35% Fe(II) after, which indicates reduction to a marginally hyper-stoichiometric magnetite surface. In contrast, XPS before and after heating the Fe_2TiO_4 film shows that the surface cannot be fully reduced by heating (Fig. 6b). XPS of the Fe_2TiO_4 film before heating shows an obvious Fe(III) satellite at ~720 eV and an Fe(II) shoulder

on the lower binding energy side of the Fe $2p^{3/2}$ core-level that is less intense relative to the Fe(III) component compared to that of the Fe_3O_4 film (Fig. 6a). Heating the Fe_2TiO_4 film to 100°C results in an increase in the Fe(II) shoulder and the development of an Fe(II) satellite along with a decrease in the Fe(III) satellite. A substantial Fe(III) component consistent with incomplete reduction remains. Even after heating to the PLD growth temperature (350 °C), an Fe(III) component is still detectable in the resulting XPS spectrum, demonstrating that it is not possible to reconstitute a completely stoichiometric Fe_2TiO_4 film surface consisting solely of Fe(II) with this approach without Mg outdiffusion from the MgO substrate, which occurs at temperatures greater than 350 °C.

Fe $L_{2,3}$-edge XAS/XMCD, having a sampling depth of ~40-50 Å, was performed for comparable analysis of the Fe_3O_4 and Fe_2TiO_4 film surface composition. Prior to analysis, the films were heated in an anoxic N_2 atmosphere glove-box (<1 ppm O_2) which, because of an intrinsically higher background O_2 partial pressure in this atmosphere relative to the high vacuum in the XPS chamber, was expected to require a higher heating temperature (300°C for 10 minutes) to achieve equivalent levels of surface reduction. Figure 7 shows normalized XAS and XMCD spectra for Fe_3O_4 (Fig. 7a) and Fe_2TiO_4 (Fig. 7b) films. The XAS and XMCD spectra for the Fe_3O_4 film have characteristics consistent with previous measurements on magnetite,[47] which for the XMCD spectrum include distinct peaks at ~708 (negative), 709 (positive), and 710 (negative) eV assigned to $Fe(II)_B$, $Fe(III)_A$, and $Fe(III)_B$, respectively. When fit with theoretical component spectra, site occupancy values are estimated as $Fe(II)_B$ (1.09): $Fe(III)_A$ (0.94): $Fe(III)_B$ (0.97), very close to the 1:1:1 relative proportions expected for stoichiometric magnetite. This finding is consistent with the XPS analysis of the as-synthesized Fe_3O_4 film, indicating a slightly hyper-stoichiometric magnetite surface after heating. For the Fe_2TiO_4 film (Fig. 7b), in

the XAS spectrum a substantial increase in the lower energy Fe(II) peak is observed, consistent with Fe(III) reduction to Fe(II) concomitant with Ti(IV) substitution into the cationic sublattice. The intensity reduction of the XMCD signal for this film, measured at 140K to account for the lower Curie temperature of Ti-rich titanomagnetites,[48-49] is in agreement with the formation of predominantly end-member ulvöspinel, in which the magnetic structure is antiferromagnetic (zero net magnetization $[Fe(II)\downarrow]_A[Fe(II)\uparrow]_BTiO_4$), with minor magnetization consistent with a titanomaghemite-like surface that persists beyond heat treatment in N_2 yielding the small but measurable XMCD signal.

As illustrated in more detail in Figure 8, XMCD of both the Fe_3O_4 and Fe_2TiO_4 films is consistent with expectations for Fe(III) to be replaced by Ti(IV) in the B sublattice and by Fe(II) in the A sublattice, producing a peak at ~707 eV in the Fe_2TiO_4 spectrum corresponding to A-site Fe(II).[30] The surface Fe/Ti ratio. calculated from the edge step of the background-subtracted Fe and Ti $L_{2,3}$-edge XAS taken consecutively at the same position on the sample, was determined to be ~1.13, which is almost identical to the value of 1.12 calculated from the atomic concentrations given by XPS after heating to 350°C. This is lower than the expected value of 2 for Fe_2TiO_4, suggesting a titanium enrichment at the surface. Consistent with our premise that the near-surface of the Ti-bearing films tend to possess titanomaghemite-like characteristics, as shown by O'Reilly[50] the mechanism of maghematization in titanomagnetites involves removal of iron from the structure leading to a reduction in the Fe/Ti ratio. However, alternative explanations cannot yet be ruled out. For example, it is also possible that the low Fe/Ti ratio is the result of a gradient within the film of Fe and Ti contents in the near-surface, with an amorphous titanium dioxide surface as the extreme case[51] but in such low concentrations that it was not be detected by Ti *K*-edge XANES.

IV. CONCLUSION

Epitaxial films of $Fe_{3-x}Ti_xO_4$ from magnetite (x=0) to ulvöspinel (x=1) were successfully grown on MgO(100) substrates by off-axis PLD. The bulk of the epitaxial films were of high structural quality, and possessed Fe/Ti ratios and a distribution of cationic oxidation states that were close to the desired composition. The films were free of secondary phases and large-domain spinodal decomposition. Ti(IV) was found to substitute predominantly for B-site Fe(III), consistent with expectations for this binary series. However, surface-sensitive spectroscopic evidence suggests that the Ti-bearing film surface (upper few nanometers) was somewhat different to the underlying bulk in terms of Fe/Ti ratio. Surface sensitive techniques such as XPS and XMCD were used to characterize this surface phase and the changes that occurred as a result of (i) oxidation upon air exposure, and (ii) reduction upon heating under vacuum or N_2 atmosphere. This work provides a foundation for production of crystallographically oriented $Fe_{3-x}Ti_xO_4$ films that can be studied for prospective device applications, or used to investigate surface reactivity and passivation of these environmentally and technologically significant materials.

ACKNOWLEDGEMENTS

This research was supported by the U.S. Department of Energy (DOE), Office of Biological and Environmental Research (OBER), as part of OBER's Subsurface Biogeochemistry Research Program (SBR). This contribution originates from the SBR Scientific Focus Area (SFA) at the Pacific Northwest National Laboratory (PNNL). Some of the research was performed in the Environmental Molecular Sciences Laboratory, a national scientific user facility sponsored by the OBER and located at PNNL. Use of the Advanced Photon Source was supported by the U.S. Department of Energy,

Office of Science, Office of Basic Energy Sciences under Contract No. DE-AC02-06CH11357. Use of the Advanced Light Source was supported by the Director, Office of Science, Office of Basic Energy Sciences, of the U.S. Department of Energy under Contract No. DE-AC02-05CH11231.

REFERENCES

1 J. D. Adam, L. E. Davis, G. F. Dionne, E. F. Schloemann, and S. N. Stitzer, Ieee Transactions on Microwave Theory and Techniques **50** (3), 721 (2002).

2 S. Picozzi and C. Ederer, J. Phys.-Condes. Matter **21** (30) (2009).

3 Y. Suzuki, Annual Review of Materials Research **31**, 265 (2001).

4 F. Bosi, U. Halenius, and H. Skogby, Am. Miner. **93** (8-9), 1312 (2008).

5 Z. Hauptman and Stephens.A, Journal of Physics E-Scientific Instruments **1** (12), 1236 (1968).

6 F. Bosi, U. Halenius, and H. Skogby, Am. Miner. **94** (1), 181 (2009).

7 V. A. M. Brabers, Physica B **205** (2), 143 (1995).

8 A. A. Cristobal, E. F. Aglietti, M. S. Conconi, and J. M. P. Lopez, Materials Chemistry and Physics **111** (2-3), 341 (2008).

9 A. A. Cristobal, E. F. Aglietti, J. M. P. Lopez, F. R. Sives, and R. C. Mercader, Journal of the European Ceramic Society **28** (14), 2725 (2008).

10 M. J. Rossiter and P. T. Clarke, Nature **207** (4995), 402 (1965).

11 A. B. Woodland and B. J. Wood, Eur. J. Mineral. **6** (1), 23 (1994).

12 A. Bollero, M. Ziese, R. Hohne, H. C. Semmelhack, U. Kohler, A. Setser, and P. Esquinazi, Journal of Magnetism and Magnetic Materials **285** (1-2), 279 (2005).

13 M. Sorescu, A. Grabias, D. Tarabasanu-Mihaila, and L. Diamandescu, Applied Surface Science **217** (1-4), 233 (2003).

14 G. D. Price, Am. Miner. **66** (7-8), 751 (1981).

15 S. A. Chambers, Surface Science Reports **39** (5-6), 105 (2000).

16 T. Kado, Thin Solid Films **459** (1-2), 187 (2004).

17 A. Nielsen, A. Brandlmaier, M. Althammer, W. Kaiser, M. Opel, J. Simon, W. Mader, S. T. B. Goennenwein, and R. Gross, Applied Physics Letters **93** (16) (2008).

18 M. L. Parames, J. Mariano, Z. Viskadourakis, N. Popovici, M. S. Rogalski, J. Giapintzakis, and O. Conde, Applied Surface Science **252** (13), 4610 (2006).

19 S. Tiwari, R. J. Choudhary, and D. M. Phase, Thin Solid Films **517** (11), 3253 (2009).

20 H. Murase, K. Fujita, S. Murai, and H. Tanaka, Journal of Physics: Conference Series **200**, 062013 (2009).

21 H. Murase, K. Fujita, S. Murai, and K. Tanaka, Materials Transactions **50** (5), 1076 (2009).

22 S. S. Perry, H. I. Kim, S. Imaduddin, S. M. Lee, and P. B. Merrill, Journal of Vacuum Science & Technology a-Vacuum Surfaces and Films **16** (6), 3402 (1998).

23 S. S. Perry and P. B. Merrill, Surface Science **383** (2-3), 268 (1997).

24 Y. Gao, Y. J. Kim, and S. A. Chambers, Journal of Materials Research **13** (7), 2003 (1998).

25 Y. J. Kim, Y. Gao, and S. A. Chambers, Surface Science **371** (2-3), 358 (1997).

26 E. S. Ilton, J. F. Boily, E. C. Buck, F. N. Skomurski, K. M. Rosso, C. L. Cahill, J. R. Bargar, and A. R. Felmy, Environ. Sci. Technol. **44** (1), 170 (2010).

27 E. Arenholz and S. O. Prestemon, Rev. Sci. Instrum. **76** (8) (2005).

28 Bradley H. Frazer, Benjamin Gilbert, Brandon R. Sonderegger, and Gelsomina De Stasio, Surface Science **537**, 161 (2003).

[29] R. A. D. Pattrick, G. Van der Laan, C. M. B. Henderson, P. Kuiper, E. Dudzik, and D. J. Vaughan, Eur. J. Mineral. **14** (6), 1095 (2002).
[30] Carolyn I. Pearce, C. Michael B. Henderson, Neil D. Telling, Richard A.D. Pattrick, John M. Charnock, Victoria S. Coker, Elke Arenholz, Floriana Tuna, and Gerrit van der Laan, Am. Miner. **95** (4), 425 (2010).
[31] G. Vanderlaan and I. W. Kirkman, J. Phys.-Condes. Matter **4** (16), 4189 (1992).
[32] G. Vanderlaan and B. T. Thole, Phys. Rev. B **43** (16), 13401 (1991).
[33] R. F. C. Farrow, P. M. Rice, M. F. Toney, R. F. Marks, J. A. Hedstrom, R. Stephenson, M. J. Carey, and A. J. Kellock, Journal of Applied Physics **93** (9), 5626 (2003).
[34] M. L. Parames, Z. Viskadourakis, M. S. Rogalski, J. Mariano, N. Popovici, J. Giapintzakis, and O. Conde, Applied Surface Science **253** (19), 8201 (2007).
[35] S. A. Chambers, S. Thevuthasan, and S. A. Joyce, Surface Science **450** (1-2), L273 (2000).
[36] B. Stanka, W. Hebenstreit, U. Diebold, and S. A. Chambers, Surface Science **448** (1), 49 (2000).
[37] R. Pentcheva, F. Wendler, H. L. Meyerheim, W. Moritz, N. Jedrecy, and M. Scheffler, Phys. Rev. Lett. **94** (12) (2005).
[38] T. Kendelewicz, P. Liu, C. S. Doyle, G. E. Brown, E. J. Nelson, and S. A. Chambers, Surface Science **453** (1-3), 32 (2000).
[39] F. de Groot, G. Vanko, and P. Glatzel, J. Phys.-Condes. Matter **21** (10) (2009).
[40] Serena DeBeer George, Patrick Brant, and Edward I. Solomon, Journal of the American Chemical Society **127** (2), 667 (2004).
[41] John Meurig Thomas and Gopinathan Sankar, Accounts of Chemical Research **34** (7), 571 (2001).
[42] D. Morris, Y. Dou, J. Rebane, C. E. J. Mitchell, R. G. Egdell, D. S. L. Law, A. Vittadini, and M. Casarin, Phys. Rev. B **61** (20), 13445 (2000).
[43] S. Aggarwal and R. Dieckmann, Physics and Chemistry of Minerals **29** (10), 695 (2002).
[44] W. X. Xu, D. R. Peacor, W. A. Dollase, R. VanDerVoo, and R. Beaubouef, Am. Miner. **82** (11-12), 1101 (1997).
[45] T. Droubay and S. A. Chambers, Phys. Rev. B **6420** (20) (2001).
[46] S. A. Krasnikov, A. S. Vinogradov, K. H. Hallmeier, R. Hohne, M. Ziese, P. Esquinazi, T. Chasse, and R. Szargan, Materials Science and Engineering B-Solid State Materials for Advanced Technology **109** (1-3), 207 (2004).
[47] C. I. Pearce, C. M. B. Henderson, R. A. D. Pattrick, G. Van der Laan, and D. J. Vaughan, Am. Miner. **91** (5-6), 880 (2006).
[48] S. Akimoto, J. Phys. Soc. Jpn. **17**, 706 (1962).
[49] Z. Kakol, J. Sabol, and J. M. Honig, Phys. Rev. B **43** (1), 649 (1991).
[50] W. Oreilly, Phys. Earth Planet. Inter. **31** (1), 65 (1983).
[51] P. Perriat, E. Fries, N. Millot, and B. Domenichini, Solid State Ionics **117** (1-2), 175 (1999).

FIGURES

FIG.1. Typical RHEED patterns obtained from an MgO(100) substrate (top) and an epitaxially-grown Fe_2TiO_4(100) film which has been exposed to oxygen (middle) and vacuum-annealed at 300°C (bottom); and a ball-and-stick model of the nominal (100) bulk truncation of Fe_2TiO_4

FIG. 2. (color online) HRXRD of the $Fe_{2.25}Ti_{0.75}O_4$/MgO(100) film (top) and the $Fe_{2.75}Ti_{0.25}O_4$/MgO(100) film (bottom) grown by pulsed laser deposition showing the shift in Bragg peak with Ti concentration.

FIG. 3. (color online) (a) Ti *K*-edge XANES spectra for films: $Fe_{2.75}Ti_{0.25}O_4$/MgO(100), $Fe_{2.50}Ti_{0.50}O_4$/MgO(100), and $Fe_{2.75}Ti_{0.25}O_4$/MgO(100). Inset shows a comparison of the Ti *K*-edge XANES of Fe_2TiO_4 and TiO_2 showing that Ti is present as Ti(IV) in Fe_2TiO_4. (b) Fe *K*-edge XANES spectra for films: $Fe_{2.75}Ti_{0.25}O_4$/MgO(100), $Fe_{2.50}Ti_{0.50}O_4$/MgO(100), $Fe_{2.75}Ti_{0.25}O_4$/MgO(100). Inset shows a comparison of the Fe *K*-edge XANES with Fe-oxide standards.

FIG. 4. (color online) (a) Fe *K*-edge XANES from Fe_3O_4 as well as Fe and Ti *K*-edge XANES from Fe_2TiO_4 indicating that Ti substitutes for Fe in the cationic sublattice. (b) Comparison of the inflection points for several $Fe_{3-x}Ti_xO_4$/MgO(100) films along with those determined for standards that shows the linear trend of Fe(III)/Fe(II) ratio with Ti concentration.

FIG. 5. (color online) Al-Kα excited XPS spectra obtained for a plasma-cleaned Fe_2TiO_4/MgO(100) film from the Fe 2*p* core-level (top), the Ti 2*p* core-level (middle), and the O 1s core-level (bottom).

FIG. 6. (color online) Al-Kα excited XPS spectra obtained for as-synthesized (a) Fe_3O_4/ MgO(100) and (b) Fe_2TiO_4/MgO(100) films from the Fe 2*p* core-level region before and after heating to different specified temperatures in the vacuum chamber.

FIG. 7. (color online) Fe $L_{2,3}$ XAS absorption spectra of an as-synthesized (a) Fe_3O_4/ MgO(100) film and (b) Fe_2TiO_4/MgO(100) film. The averaged *L*-edge spectra were collected in a reversible 0.6 Tesla magnetic field at 140K, and the resulting XMCD difference spectra are shown below.

FIG. 8. (color online) Fe $L_{2,3}$-edge XMCD spectra for a Fe_3O_4/ MgO(100) film (black curve) and a Fe_2TiO_4/MgO(100) film (red curve; intensity increased by a factor of twelve for comparison).

(a)

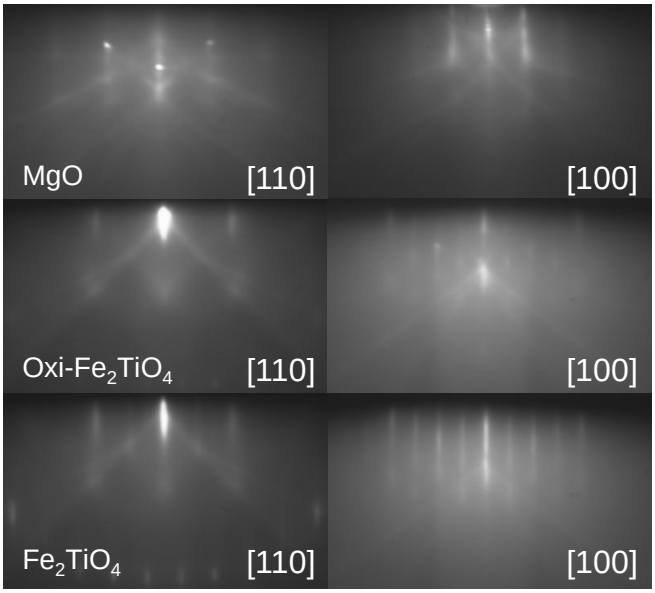

(b)

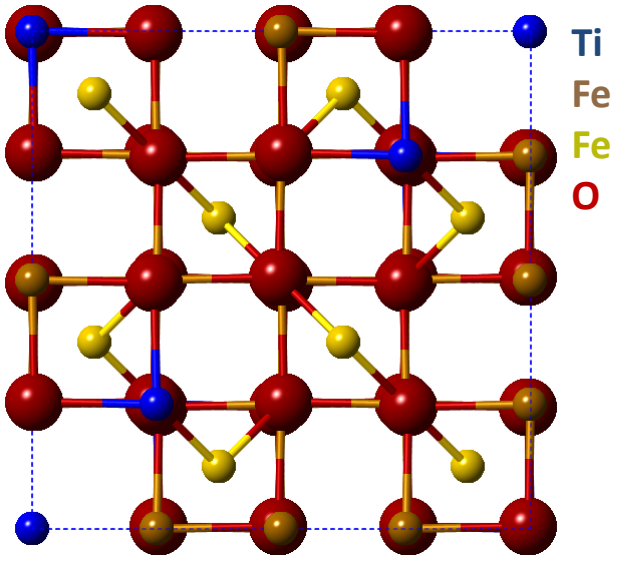

Fig. 1.
Droubay *et al*. PRB

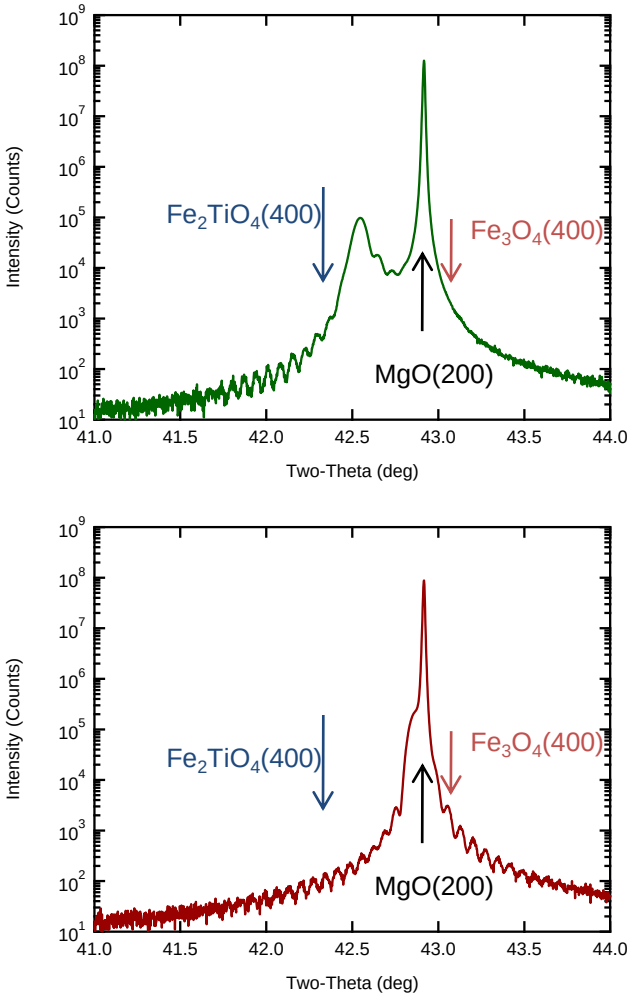

Fig. 2.
Droubay *et al*. PRB

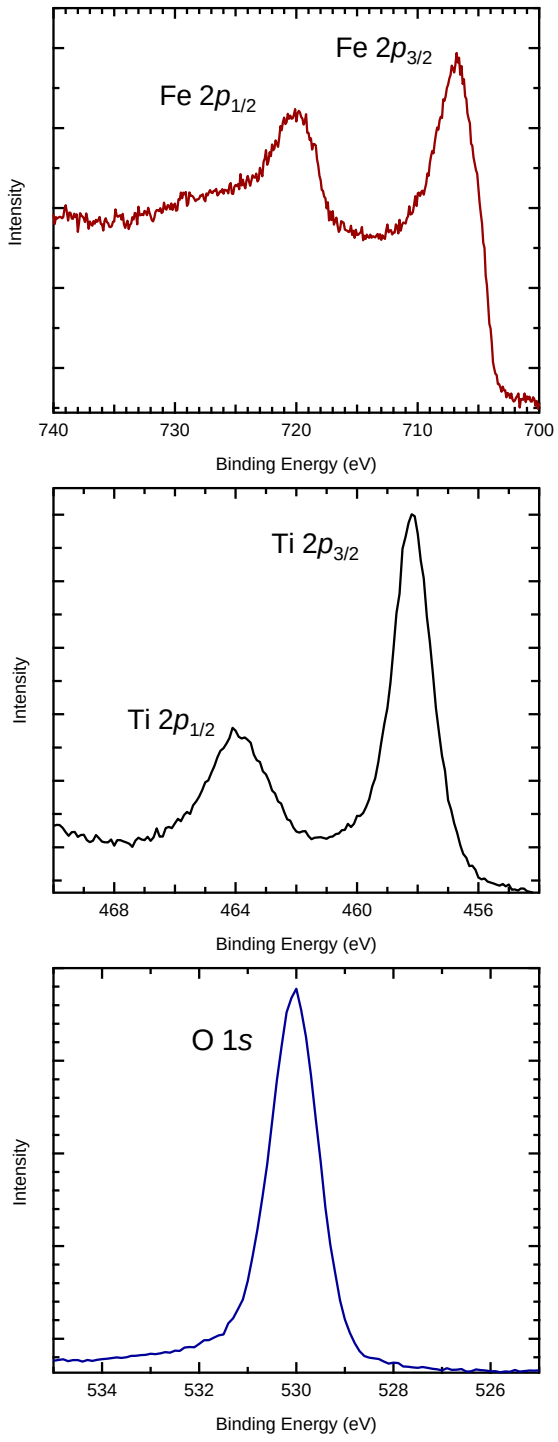

Fig. 3.
Droubay *et al*. PRB

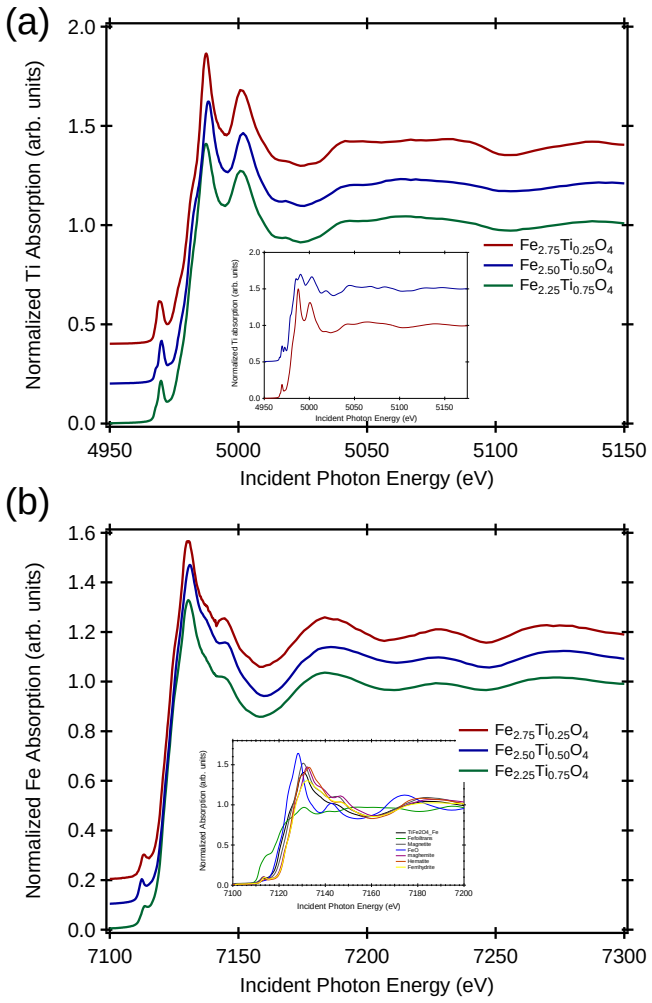

Fig. 4.
Droubay *et al*. PRB

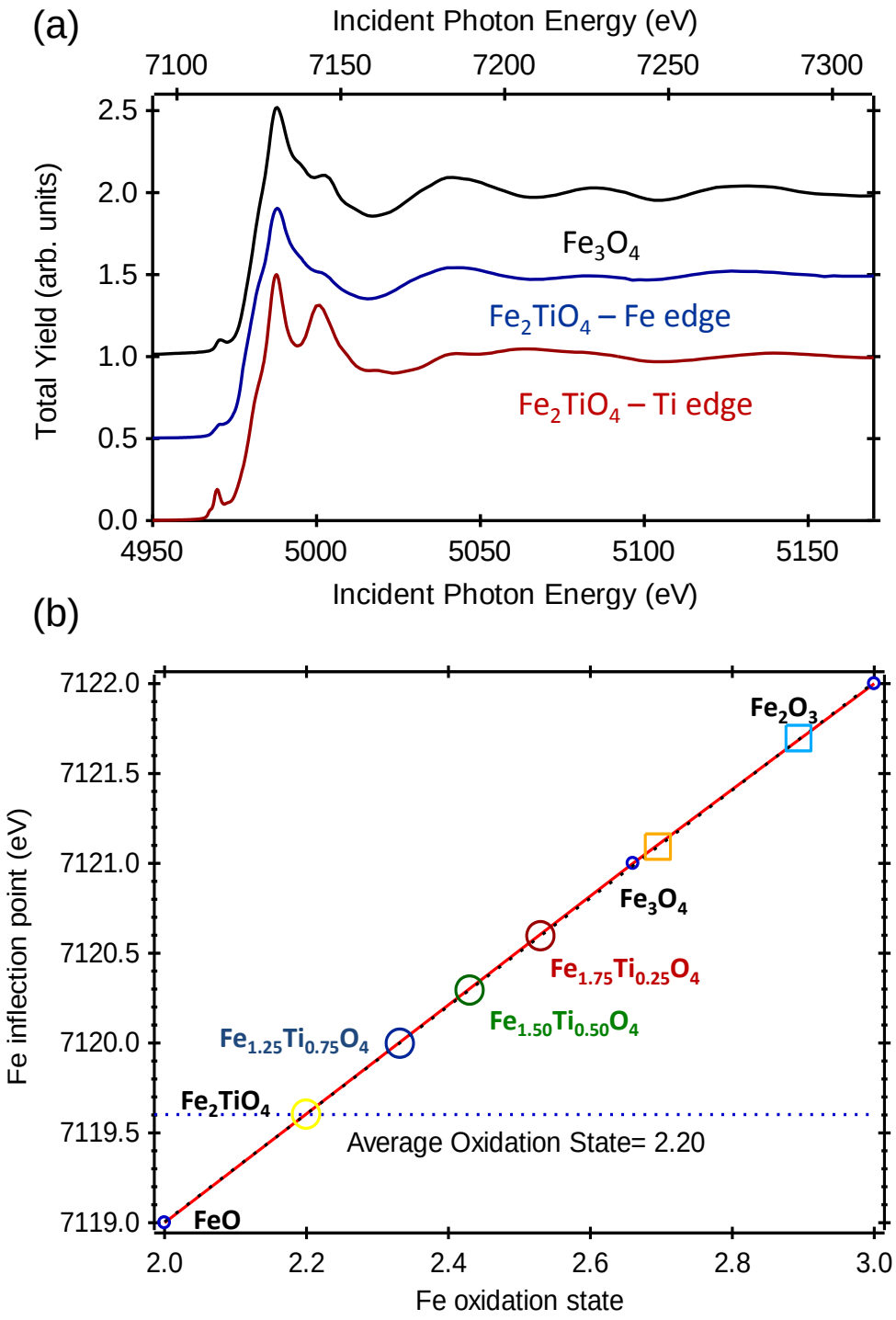

Fig. 5.
Droubay *et al*. PRB

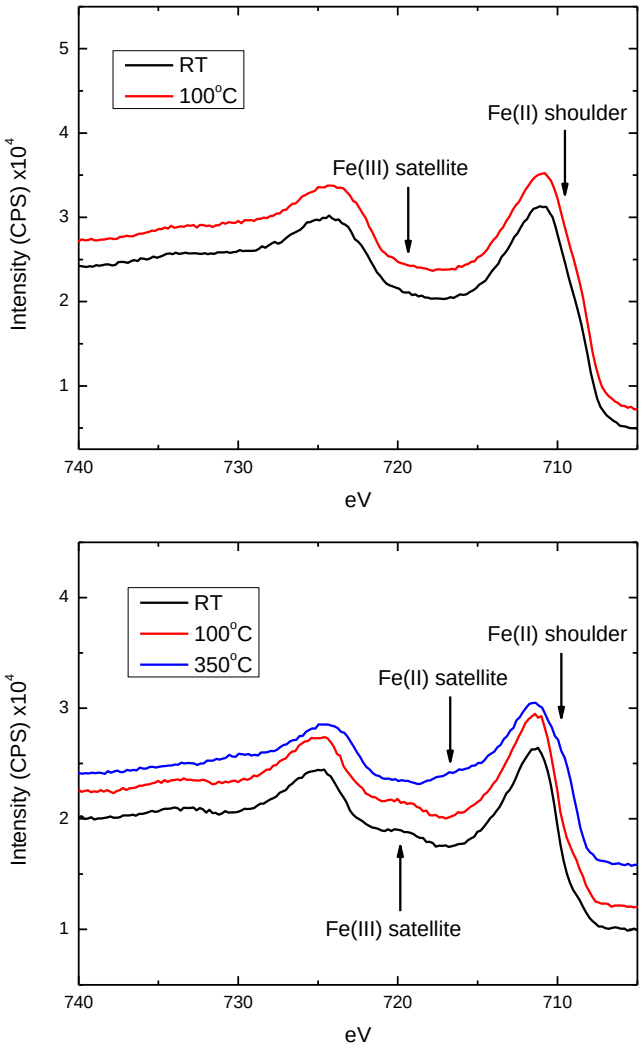

Fig. 6.
Droubay *et al*. PRB

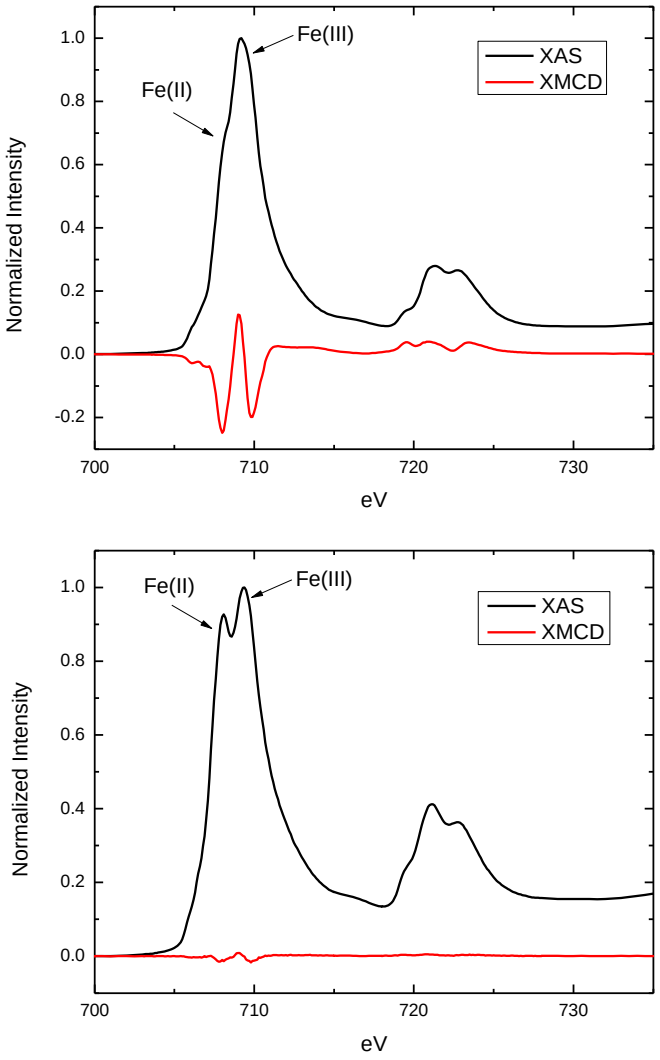

Fig. 7.
Droubay *et al*. PRB

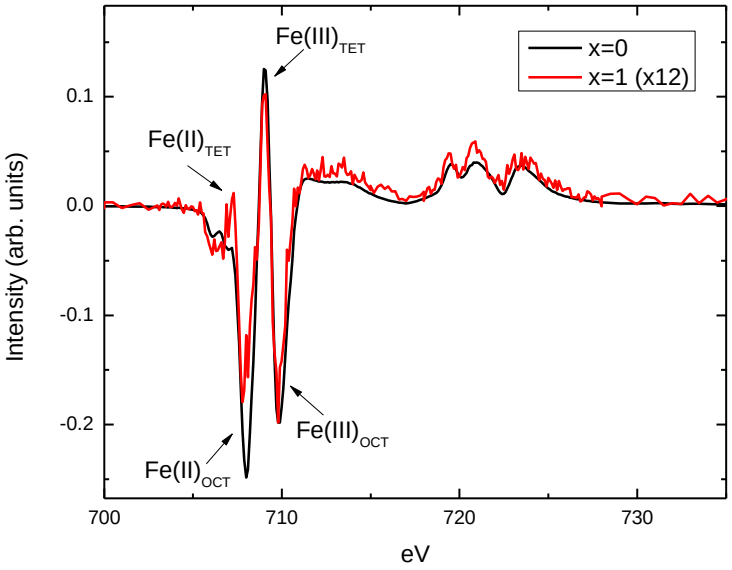

Fig. 8.
Droubay *et al*. PRB